

pubs.acs.org/JPCL Letter

# Coherent Phonon Dynamics in Plasmonic Gold Tetrahedral Nanoparticle Ensembles

Bailey M. Chandler, Diptesh Dey, Yi Wang, Xingchen Ye, George C. Schatz, Lin X. Chen, and Richard D. Schaller\*



Cite This: J. Phys. Chem. Lett. 2024, 15, 9686-9691



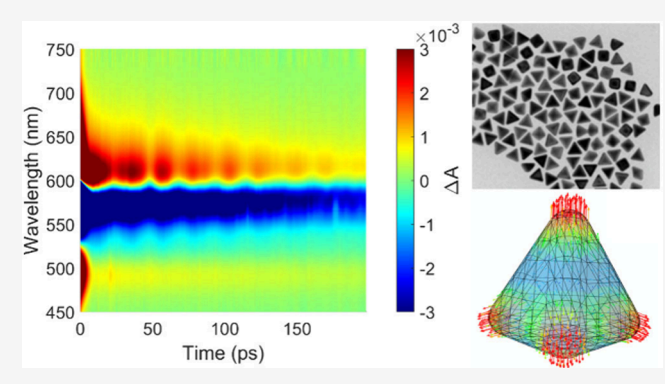
**ACCESS** I

III Metrics & More

Article Recommendations

sı Supporting Information

ABSTRACT: Coherent phonon modes supported by plasmonic nanoparticles offer prospective applications in chemical and biological sensing. Whereas the characterization of these phonon modes often requires single-particle measurements, synthetic routes to narrow size distributions of nanoparticles permit ensemble investigations. Recently, the synthesis of highly monodisperse gold tetrahedral nanoparticles with tunable edge lengths and corner sharpnesses has been developed. Herein, we characterize a size series of these nanoparticles in colloidal dispersion via transient absorption spectroscopy to examine their mechanical and plasmonic responses upon photoexcitation. Oscillations of transient absorption signals are observed in the plasmon resonance and correspond to the lowest-order radial



breathing modes of the nanoparticles, the frequencies of which are affected by the edge length and truncation of the corners. Homogeneous quality factor values ranging from 24 to 34 are observed for the oscillations that convey potential utility in mass-sensing and plasmon-exciton-coupling photonics schemes. Finite-difference time domain and finite element analysis calculations establish specific optically relevant phonon modes.

plasmonic metal nanoparticles which support coherent phonon modes are of high interest for chemical and biological sensing, 1-7 high-resolution optical imaging, 8,9 and optomechanical applications. 10,11 The localized surface plasmon resonance (LSPR), wherein conduction band electrons collectively oscillate at a frequency resonant with an incident electromagnetic field, dominates the optical properties of these nanoparticles over an appreciable size range. The position of the LSPR can be tuned from ultraviolet to near-infrared ranges via synthetic control of metal nanoparticle composition, size, and shape. 1,4,12-16 These same particle properties additionally affect the phonon frequency and degree of mechanical deformation of the nanoparticle lattice. For particles where phonon-driven lattice deformation couples with their optical resonance, coherent acoustic phonons can be observed in timeresolved optical studies as oscillatory shifts of the LSPR position. Upon photon absorption, electrons are promoted into a nonequilibrium distribution and undergo electron scattering processes on the femtosecond scale. 12-17 Electron-phonon coupling processes then distribute this energy through the metal lattice, resulting in periodic expansion and contraction of the finite particle. When lattice heating occurs on a time scale shorter than that of the acoustic mode period, these phonons can be launched coherently. 12–18 Polydispersity in an ensemble sample can significantly impede observation of such oscillations and yield observed dephasing times that limit

phonon characterization and prospective utility. <sup>18</sup> This may be circumvented via either single-particle studies or the synthesis of highly monodisperse samples.

Although synthetic routes for many gold nanoparticle shapes have been well-established, the synthesis of highly monodisperse tetrahedral nanoparticles has remained elusive. This was in part due to lower symmetry than, for example, sphere, making growth thermodynamically unfavorable. <sup>19</sup> Zheng and co-workers demonstrated that highly monodisperse gold nanotetahedra could be achieved using a spherical gold seed paired with precise kinetic control of the reaction. <sup>19</sup> The edge length and degree of truncation at the tips can be manipulated by this synthetic route. More recently, these nanoparticles have been used as building blocks for nanocrystal superstructures, even in some cases inducing chirality. <sup>20–23</sup>

In addition to an expected red shift of the LSPR as nanoparticle size increases, static characterizations of gold tetrahedra nanoparticle optical properties have shown that

Received: July 21, 2024
Revised: September 9, 2024
Accepted: September 12, 2024
Published: September 17, 2024





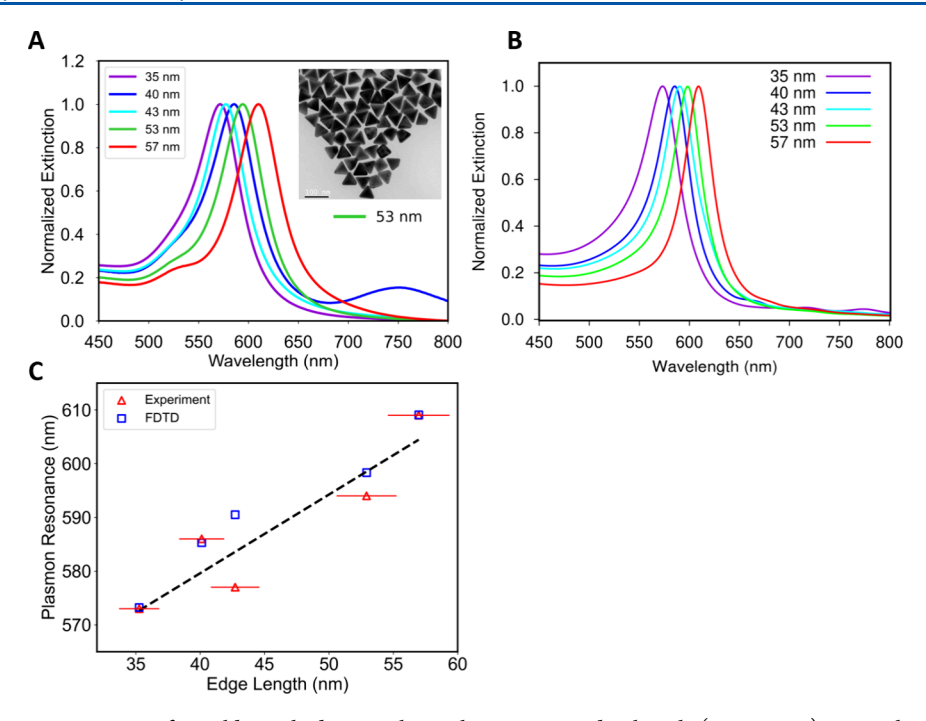


Figure 1. (A) Static extinction spectra for gold tetrahedra samples with increasing edge length (35–57 nm). Note that varied edge sharpness impacts trend systematicity. The inset shows a TEM image of the 53 nm sample (100 nm scale bar). (B) Static extinction spectra from FDTD calculations. (C) Maximum intensity of plasmon resonance as a function of edge length determined from experiment and theory. Dashed line represents linear fit of experimental data; error bars represent standard deviation from ensemble measurements.

sharper corners shift the LSPR position an additional ~10 nm, independent of edge length, in comparison to rounded corners. Experimental data have also revealed that sharp corners can yield an additional shoulder extinction peak of higher energy than the LSPR. Theoretical studies have indicated this additional peak may result from dipole—quadrupole resonance coupling, due to changes in electron density at the corners. Transient optical properties and coherent phonon behavior of tetrahedral nanoparticles heretofore were unexplored. In particular, one or more modes of acoustic distortion of these particles can yield complex oscillatory behavior.

Here, we use transient absorption and theoretical modeling to examine the time-dependent response of a size series of gold tetrahedra, observe coherent phonons, and examine the evolution of detected frequencies as a function of nanoparticle size and corner truncation. Experimentally observed oscillations were fit to yield the lowest breathing mode frequency of each sample, which is well separated in frequency from additional vibrational modes as well as the quality factor of the ensemble. Continuum mechanics calculations based on the finite element method were performed to determine the lowest-order radial mode of each nanoparticle size, representative of the breathing mode that was observed in transient absorption experiments. Edge length and corner truncation offer two variables for synthetic tuning of the LSPR wavelength and phonon frequencies.

A size series of gold nanotetrahedra with varying edge lengths (referred to herein by edge length) and corner sharpness were characterized via transmission electron microscopy (TEM) and static extinction (for dispersions in water) as shown in Figure 1A. Both the TEM images (example shown in the inset) and the narrow line widths of the LSPR peaks convey that the samples are highly monodisperse, with average edge length dispersity of  $\pm 4.4\%$ . The narrow

dispersions reduce inhomogeneous damping, which aids in detecting the influence of optically coupled phonon modes. LSPR peaks of the five samples span a spectral region from 570 to 610 nm, with the edge lengths of the nanoparticles ranging from 35 to 57 nm. The 40 nm sample shows an additional broad peak around 750 nm, possibly as a result of some particle aggregation. The 40 and 57 nm samples exhibit sharper tips than the other samples based on the ratio of projected edge length versus measured edge length, as detailed in the Supporting Information (SI). These samples show an additional shoulder peak at ~510 nm, possibly due to dipolequadrupole plasmon coupling proposed in theoretical calculations as a result of sharper corners.<sup>24</sup> As expected, longer edge lengths lead to a red shift in the peak position of the plasmon resonance. Finite-difference time-domain (FDTD) calculations using Lumerical software were performed using the particle dimensions determined by TEM (Table S1), and static extinction spectra based on FDTD are presented in Figure 1B. As the nanoparticles were modeled with 6 or 7 nm rounding at the tips, the FDTD calculations were unable to capture the secondary shoulder peak in the samples with sharper tips. Regardless, these calculations still demonstrate the expected increasing trend of the LSPR wavelength as particle size increases. Figure 1C shows the LSPR wavelength as a function of edge length fit to a linear regression model. As corner sharpness also impacts LSPR position, the data was additionally fit only considering samples with rounded corners, with edge lengths of 35, 43, and 53 nm. The plasmon resonance of the 40 and 57 nm samples was shifted by an additional ~10 nm to redder wavelengths from what is predicted by the trend line when only samples with rounded corners are considered. Notably, the LSPR position of the 40 nm sample is at a longer wavelength than that of the 43 nm sample as a result of its sharper corners, despite having a slightly shorter edge length.

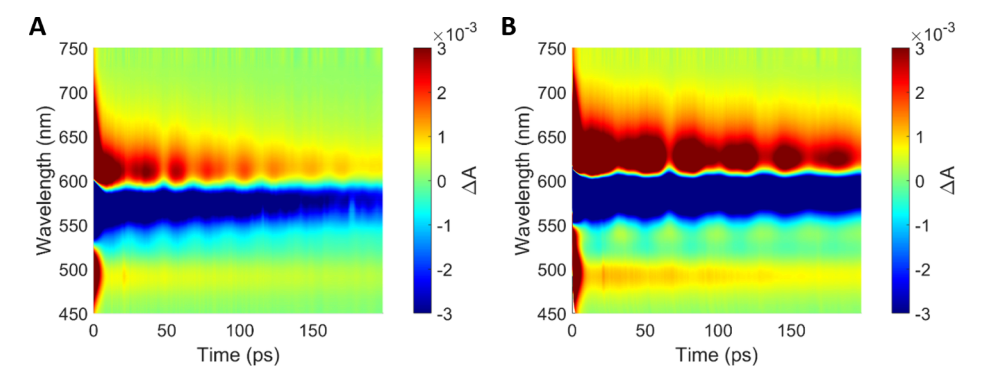


Figure 2. 2D transient absorption maps for the (A) 35 nm and (B) 53 nm edge-length samples, each excited at 570 nm. Oscillatory features from phonon modes are evident, with the larger 53 nm sized samples exhibiting longer-period oscillations.

Femtosecond transient absorption measurements using a pump pulse tuned to resonance with the lowest-energy LSPR (near 570 nm) were performed to characterize the ultrafast optical response of all samples. It is not anticipated that higherenergy excitation at the shoulder peak arising from quadrupole—dipole coupling in the samples with sharper tips should change the observable phonon mode behavior. Following rapid electron—electron and electron—phonon scattering, distinct oscillations at the position of the plasmon resonance energy convey that coherent phonons are impulsively excited. Oscillatory spectral response is consistent with the sensitivity of the plasmon to repetitive expansion and contraction of the lattice.

The 2D transient absorption maps, shown in Figure 2, exhibit long-lived transients with distinct and persistent oscillations. The plasmon resonance shifts to a longer wavelength upon heating, resulting in a bleach where extinction intensity is reduced, as is commonly observed in plasmonic nanoparticles. Oscillatory features on the blue versus red side of the LSPR undergo a 180-degree phase shift as the signal goes from a bleach to an absorption feature, as expected due to shifts in the LSPR between the redder and bluer wavelengths. The population dynamics follows initial electron—phonon coupling processes, wherein heat is transferred to the lattice, followed by phonon—phonon coupling. These dynamics were modeled as follows:

$$y(t) = G(t) \Sigma A_i e^{-t/\tau_i}$$

where G(t) is a Gaussian that is used to deconvolute the instrument response function, t is the pump—probe time delay,  $\tau_i$  is the i-th decay time constant, and  $A_i$  is a pre-exponential amplitude. To evaluate the phonon mode frequency and dephasing times, exponential decay dynamics were first subtracted from kinetic traces and fast Fourier transforms (FFTs) were then performed on the residuals with oscillatory features. Using the results from FFT as initial parameters, the traces (ignoring early times, <20 ps) were fit to a summation of exponentially decaying cosine functions as follows:

$$\sum A_i \exp\left(\frac{-t}{\tau_{1i}}\right) \exp\left(-\left(\frac{t}{\tau_{2i}}\right)^2\right) \cos\left(\frac{2\pi t}{T_i} + \phi_i\right)$$

where A is the amplitude,  $\tau_1$  is the homogeneous lifetime,  $\tau_2$  is the inhomogeneous lifetime due to size polydispersity, T is the period, and  $\varphi$  is the phase constant. The inhomogeneous lifetimes were determined using the measurements from TEM images, and further details for these calculations are provided

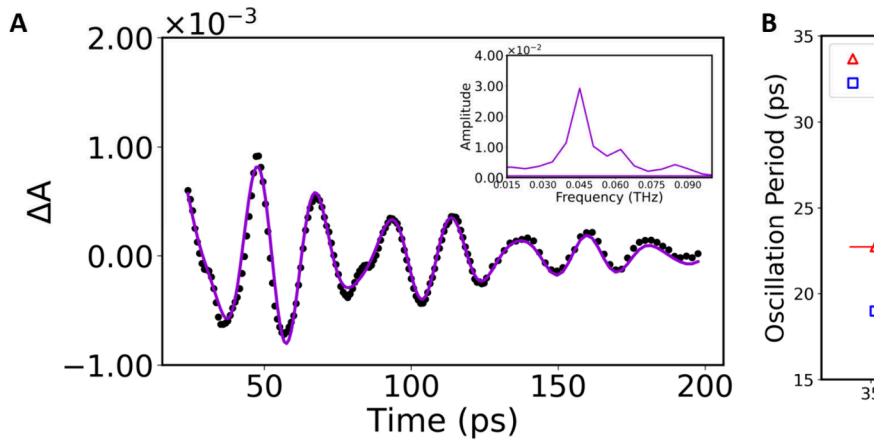
in the SI. Numerical results for these fits are presented in Table 1. This processing resulted in the distinct identification of a

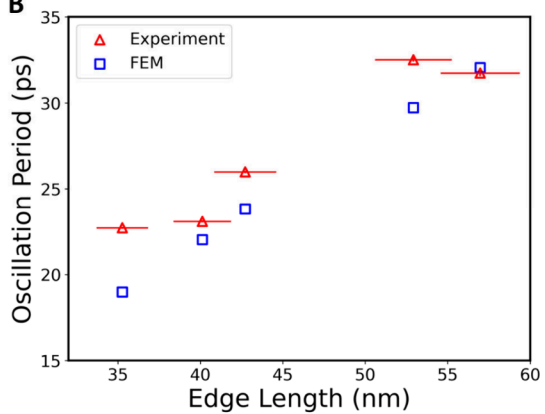
Table 1. Primary Phonon Period, Homogeneous Lifetime, and Inhomogeneous Lifetime Calculated from Fitting Experimental Oscillatory Kinetic Traces

Edge Length (nm)	Homogeneous Lifetime $\tau_1$ (ps)	Inhomogeneous Lifetime $\tau_2$ (ps)	Primary Phonon Period (ps)
$35 \pm 1.6$	$230 \pm 9$	$116 \pm 0.2$	$23 \pm 0.05$
$40 \pm 1.7$	$179 \pm 6$	$119 \pm 0.2$	$23 \pm 0.09$
$43 \pm 1.9$	$285 \pm 20$	$132 \pm 0.2$	$26 \pm 0.1$
$53 \pm 2.3$	$351 \pm 23$	$167 \pm 0.2$	$32 \pm 0.1$
$57 \pm 2.4$	$323 \pm 16$	$170 \pm 0.2$	$32\pm0.2$

primary oscillation frequency. In addition to a primary oscillation frequency, FFTs for each sample also showed a weaker secondary peak; this was accounted for by fitting the oscillatory kinetic traces with a summation of two damped harmonics as opposed to one. The comparatively complex shape of these structures makes evaluation of the primary oscillation frequency difficult. While the predominant period extracted is due to the radial breathing mode, the presence of additional weaker frequencies may be the result of overtone phonon modes, as detailed further in the SI. An FFT and example fit for the 35 nm sample evaluated at 605 nm are shown in Figure 3A. The primary oscillatory period extracted from these fits follows a linear trend with increasing edge length, shown in Figure 3B. Disparities in the trend may be the result of variable corner truncation, as the 40 and 57 nm samples, which have sharper corners, exhibited oscillatory periods 1.4 and 1.1 ps shorter, respectively, than the overall trend predicted by the linear regression model. When only considering samples with rounded corners in the linear model, these differences became 2 and 2.8 ps shorter, respectively, demonstrating that corner sharpness has a notable impact on both the LSPR position and phonon frequencies for these

A finite-element method (FEM) based on Abaqus software was utilized to calculate the fundamental radial breathing mode frequencies for the given samples. The nanoparticles were modeled as regular tetrahedra by using the projected edge length from TEM images and 5 nm rounded tips. It has previously been demonstrated for tetrahedral shapes that the lowest-order radial mode extracted from FEM calculations corresponds to the breathing mode and there is a weak sensitivity of the frequencies to rounded tips, so we assume 5





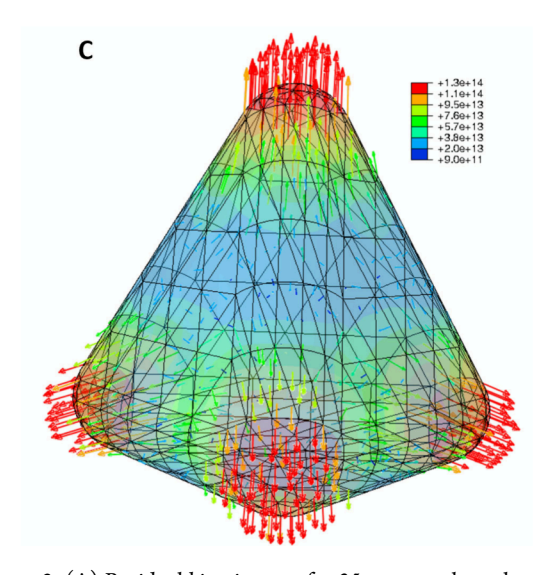
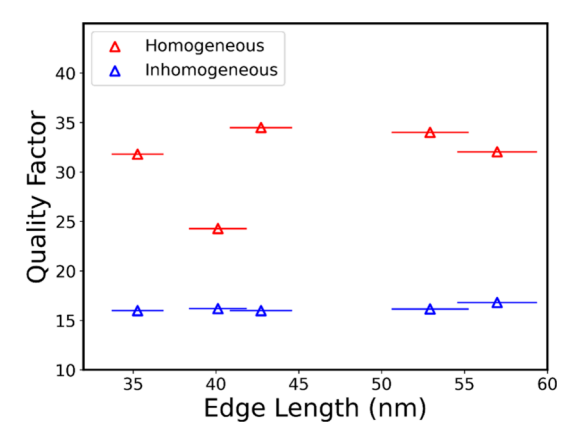


Figure 3. (A) Residual kinetic trace for 35 nm sample evaluated at 605 nm fitted with summation of two exponentially decaying cosine waves. The inset shows a fast Fourier transform of the kinetic trace. (B) Oscillation period for the fundamental breathing mode measured experimentally (red) and calculated by FEM simulations (blue). (C) Simulation of the radial breathing mode; color bar indicates magnitude of outward expansion. Red arrows at the tips indicate points of greatest outward expansion.

nm instead of 6 or 7 nm roundings.<sup>26</sup> The calculated frequencies for this mode are plotted against the experimental frequencies in Figure 3B, with Figure 3C depicting the expansion and contraction of the nanoparticle lattice. The greatest magnitude of outward expansion occurs at the nanoparticle tips, as indicated by the red arrows. These calculations most closely match the samples with sharper tips, while showing a slightly increased frequency for the samples with rounded tips. This slight discrepancy likely arises due to differences in corner truncation between experimental and modeled samples. These calculations support the previous conclusion that these oscillations originate from the lowestorder radial breathing mode. The inset of Figure 3A suggests that a higher-frequency acoustic mode near 0.062 THz also contributes to the experimental results. In the Supporting Information we present an analysis of the theory/experiment comparison for this face-displacement breathing mode.

As both the homogeneous damping time and phonon frequency are dependent on nanoparticle size, the quality factor is considered for a more apt comparison of oscillations with other sample types. The quality factor is defined as  $Q_i = Q_i = \frac{\pi r_1}{T}$ , using the homogeneous lifetime extracted previously.<sup>25,27</sup>

The homogeneous Q-factors for each samples' primary phonon breathing mode were calculated to range from 24.3 to 34.5, while the inhomogeneous Q-factors range from 15.9 to 16.8. The homogeneous and inhomogeneous Q-factors versus edge lengths are presented in Figure 4. It is notable that samples with higher quality factors exhibit longer homogeneous lifetimes. The 40 nm sample may have a somewhat lower homogeneous Q-factor as a result of sample aggregation, as indicated in the static absorption spectrum. It is also important to note the homogeneous lifetimes obtained from the residual kinetic trace fits are longer than the experimental time window, which could introduce some error into the fits. As the inhomogeneous Q-factors were derived directly from TEM images, they are much more accurate. Gold bipyramids have been previously demonstrated to have homogeneous Q-factors ranging from 10 to 30 for samples in water and methanol, with variations due to differences in morphology and surface roughness between samples. 25,28,29 It should also be noted that quality factor is solvent dependent, and here all samples were measured as dispersions in water. The viscosity of the solvent can greatly alter the rate of homogeneous damping and subsequently the quality factor; previous studies have shown



**Figure 4.** Homogeneous and inhomogeneous *Q*-factors versus edge length.

that gold bipyramids dispersed in viscous solvents such as ethylene glycol exhibit much lower quality factors compared to bipyramids dispersed in water. Gold nanotetrahedra thus offer a comparable alternative for mass sensing applications due to their similar quality factors and long damping times. Additional studies could be performed to determine the phonon behavior of gold nanotetrahedra in different solvents and longer time windows.

In summary, the coherent acoustic phonons of a series of gold tetrahedral nanoparticle ensembles measured as colloidal dispersions were characterized by transient absorption spectroscopy. The phonon mode frequencies of these nanoparticles can be tuned via both edge length and corner sharpness. Tunability of the LSPR and phonon frequencies offers advantages in biological and chemical mass sensing applications as well as high-resolution imaging based on detected phonon modes. These findings further serve as a starting point for future research in analyzing the optomechanical properties of 2D or 3D superlattices, which have been formed using these tetrahedral nanoparticles as building blocks.

## ASSOCIATED CONTENT

#### Supporting Information

The Supporting Information is available free of charge at https://pubs.acs.org/doi/10.1021/acs.jpclett.4c02146.

Gold tetrahedral nanoparticle synthesis, transient absorption method, evaluation of inhomogeneous damping, FDTD and FEM computational details, and description of other vibrational mode (PDF)

## AUTHOR INFORMATION

### **Corresponding Author**

Richard D. Schaller — Department of Chemistry,
Northwestern University, Evanston, Illinois 60208, United
States; Center for Nanoscale Materials, Argonne National
Laboratory, Lemont, Illinois 60439, United States;
International Institute for Nanotechnology; Paula M.
Trienens Institute for Sustainability and Energy,
Northwestern University, Evanston, Illinois 60208, United
States; orcid.org/0000-0001-9696-8830;
Email: schaller@northwestern.edu, schaller@anl.gov

#### **Authors**

Bailey M. Chandler – Department of Chemistry, Northwestern University, Evanston, Illinois 60208, United States

Diptesh Dey — Department of Chemistry, Northwestern University, Evanston, Illinois 60208, United States;
ocid.org/0000-0002-1906-9580

Yi Wang — Department of Chemistry, Indiana University, Bloomington, Indiana 47405, United States; orcid.org/ 0000-0003-2882-8777

Xingchen Ye — Department of Chemistry, Indiana University, Bloomington, Indiana 47405, United States; ● orcid.org/0000-0001-6851-2721

George C. Schatz – Department of Chemistry, Northwestern University, Evanston, Illinois 60208, United States; orcid.org/0000-0001-5837-4740

Lin X. Chen — Department of Chemistry, Northwestern University, Evanston, Illinois 60208, United States; Chemical Sciences and Engineering Division, Argonne National Laboratory, Lemont, Illinois 60439, United States;

ocid.org/0000-0002-8450-6687

Complete contact information is available at: https://pubs.acs.org/10.1021/acs.jpclett.4c02146

#### Notes

The authors declare no competing financial interest.

#### ACKNOWLEDGMENTS

We acknowledge support from the Ultrafast Initiative of the U.S. Department of Energy, Office of Science, Office of Basic Energy Sciences, through Argonne National Laboratory under Contract No. DE-AC02-06CH11357. Use of the Center for Nanoscale Materials, an Office of Science user facility, was supported by the U.S. Department of Energy, Office of Science, Office of Basic Energy Sciences, under Contract No. DE-AC02-06CH11357. D.D. and G.C.S. were supported by the US Department of Energy, Office of Basic Energy Sciences, under Grant No. DE-SC0004752. Y.W. and X.Y. were supported by the U.S. National Science Foundation under award CHE-2239441. D.D. thanks Clotilde Lethiec and Jeffrey Paci for valuable guidance.

# REFERENCES

- (1) Willets, K. A.; Van Duyne, R. P. Localized Surface Plasmon Resonance Spectroscopy and Sensing. *Annu. Rev. Phys. Chem.* **2007**, *58*, 267–297.
- (2) Loiseau, A.; Asila, V.; Boitel-Aullen, G.; Lam, M.; Salmain, M.; Boujday, S. Silver-Based Plasmonic Nanoparticles for and Their Use in Biosensing. *Biosensors* **2019**, *9* (2), 78.
- (3) Arlett, J. L.; Myers, E. B.; Roukes, M. L. Comparative advantages of mechanical biosensors. *Nat. Nanotechnol.* **2011**, *6* (4), 203–215.
- (4) Stewart, M. E.; Anderton, C. R.; Thompson, L. B.; Maria, J.; Gray, S. K.; Rogers, J. A.; Nuzzo, R. G. Nanostructured Plasmonic Sensors. *Chem. Rev.* **2008**, *108* (2), 494–521.
- (5) Mejía-Salazar, J. R.; Oliveira, O. N., Jr Plasmonic Biosensing. *Chem. Rev.* **2018**, *118* (20), 10617–10625.
- (6) Stanley, R. Plasmonics in the mid-infrared. *Nat. Photonics* **2012**, 6 (7), 409–411.
- (7) Zeng, S.; Baillargeat, D.; Ho, H.-P.; Yong, K.-T. Nanomaterials enhanced surface plasmon resonance for biological and chemical sensing applications. *Chem. Soc. Rev.* **2014**, 43 (10), 3426.
- (8) Fuentes-Domínguez, R.; Pérez-Cota, F.; Naznin, S.; et al. Super-resolution imaging using nano-bells. Sci. Rep 2018, 8, 16373.

- (9) Fuentes-Domínguez, R.; Naznin, S.; La Cavera, S., III; Cousins, R.; Pérez-Cota, F.; Smith, R. J.; Clark, M. Polarization-Sensitive Super-Resolution Phononic Reconstruction of Nanostructures. *ACS Photonics* **2022**, *9* (6), 1919–1925.
- (10) Lin, K.-H.; Lai, C.-M.; Pan, C.-C.; Chyi, J.-I.; Shi, J.-W.; Sun, S.-Z.; Chang, C.-F.; Sun, C.-K. Spatial manipulation of nanoacoustic waves with nanoscale spot sizes. *Nat. Nanotechnol.* **2007**, 2 (11), 704–708.
- (11) Cunha, J.; Guo, T.-L.; Della Valle, G.; Koya, A. N.; Proietti Zaccaria, R.; Alabastri, A. Controlling Light, Heat, and Vibrations in Plasmonics and Phononics. *Adv. Opt. Mater.* **2020**, *8* (24), 2001225.
- (12) Hartland, G. V. Optical Studies of Dynamics in Noble Metal Nanostructures. *Chem. Rev.* **2011**, *111* (6), 3858–3887.
- (13) Hartland, G. V. Coherent Excitation of Vibrational Modes in Metallic Nanoparticles. *Annu. Rev. Phys. Chem.* **2006**, *57* (1), 403–430
- (14) Hartland, G. V. Coherent vibrational motion in metal particles: Determination of the vibrational amplitude and excitation mechanism. *J. Chem. Phys.* **2002**, *116* (18), 8048–8055.
- (15) Link, S.; El-Sayed, M. A. Optical Properties and Ultrafast Dynamics of Metallic Nanocrystals. *Annu. Rev. Phys. Chem.* **2003**, *54* (1), 331–366.
- (16) Jeong, S.; Liu, Y.; Zhong, Y.; Zhan, X.; Li, Y.; Wang, Y.; Cha, P. M.; Chen, J.; Ye, X. Heterometallic Seed-Mediated Growth of Monodisperse Colloidal Copper Nanorods with Widely Tunable Plasmonic Resonances. *Nano Lett.* **2020**, *20* (10), 7263–7271.
- (17) Ostovar, B.; Su, M.-N.; Renard, D.; Clark, B. D.; Dongare, P. D.; Dutta, C.; Gross, N.; Sader, J. E.; Landes, C. F.; Chang, W.-S.; et al. Acoustic Vibrations of Al Nanocrystals: Size, Shape, and Crystallinity Revealed by Single-Particle Transient Extinction Spectroscopy. J. Phys. Chem. A 2020, 124 (19), 3924–3934.
- (18) Huang, W.; Qian, W.; El-Sayed, M. A. Coherent Vibrational Oscillation in Gold Prismatic Monolayer Periodic Nanoparticle Arrays. *Nano Lett.* **2004**, *4* (9), 1741–1747.
- (19) Zheng, Y.; Liu, W.; Lv, T.; Luo, M.; Hu, H.; Lu, P.; Choi, S.-I.; Zhang, C.; Tao, J.; Zhu, Y.; et al. Seed-Mediated Synthesis of Gold Tetrahedra in High Purity and with Tunable, Well-Controlled Sizes. *Chem.—Asian J.* **2014**, *9* (9), 2635–2640.
- (20) Wang, Y.; Chen, J.; Zhong, Y.; Jeong, S.; Li, R.; Ye, X. Structural Diversity in Dimension-Controlled Assemblies of Tetrahedral Gold Nanocrystals. *J. Am. Chem. Soc.* **2022**, *144* (30), 13538–13546.
- (21) Wang, Y.; Chen, J.; Li, R.; Götz, A.; Drobek, D.; Przybilla, T.; Hübner, S.; Pelz, P.; Yang, L.; Apeleo Zubiri, B.; et al. Controlled Self-Assembly of Gold Nanotetrahedra into Quasicrystals and Complex Periodic Supracrystals. *J. Am. Chem. Soc.* **2023**, *145* (32), 17902–17911.
- (22) Zhou, S.; Li, J.; Lu, J.; Liu, H.; Kim, J.; Kim, A.; Yao, L.; Liu, C.; Qian, C.; Hood, Z.; Lin, X.; Chen, W.; Gage, T.; Arslan, I.; Travesset, A.; Sun, K.; Kotov, N.; Chen, Q. Chiral Assemblies of Pinwheel Superlattices on Substrates. *Nature* **2022**, *612*, 259–265.
- (23) Cheng, Z.; Jones, M. R. Assembly of planar chiral superlattices from achiral building blocks. *Nat. Commun.* **2022**, *13* (1), 4207.
- (24) Zheng, P.; Paria, D.; Wang, H.; Li, M.; Barman, I. Optical properties of symmetry-breaking tetrahedral nanoparticles. *Nanoscale* **2020**, *12* (2), 832–842.
- (25) Kirschner, M. S.; Lethiec, C. M.; Lin, X.-M.; Schatz, G. C.; Chen, L. X.; Schaller, R. D. Size-Dependent Coherent-Phonon Plasmon Modulation and Deformation Characterization in Gold Bipyramids and Nanojavelins. *ACS Photonics* **2016**, *3* (5), 758–763.
- (26) Lethiec, C. M.; Madison, L. R.; Schatz, G. C. Dependence of Plasmon Energies on the Acoustic Normal Modes of  $Ag_n$  (n = 20, 84, and 120) Clusters. *J. Phys. Chem. C* **2016**, 120, 20572–20578.
- (27) Soavi, G.; Tempra, I.; Pantano, M. F.; Cattoni, A.; Collin, S.; Biagioni, P.; Pugno, N. M.; Cerullo, G. Ultrasensitive Characterization of Mechanical Oscillations and Plasmon Energy Shift in Gold Nanorods. *ACS Nano* **2016**, *10* (2), 2251–2258.
- (28) Pelton, M.; Sader, J.; Burgin, J.; et al. Damping of acoustic vibrations in gold nanoparticles. *Nat. Nanotechnol.* **2009**, *4*, 492–495.

(29) Dacosta Fernandes, B.; Spuch-Calvar, M.; Baida, H.; Tréguer-Delapierre, M.; Oberlé, J.; Langot, P.; Burgin, J. Acoustic Vibrations of Au Nano-Bipyramids and their Modification under Ag Deposition: a Perspective for the Development of Nanobalances. *ACS Nano* **2013**, 7 (9), 7630–7639.